Article:

Button, C.A. orcid.org/0009-0005-2070-9548, Mantheakis, E., Wang, G. orcid.org/0000-0003-0125-454X et al. (1 more author) (2025) Effect of pressure, temperature, and particle size on cold sintered ZnO for transparent thick films on polymer substrates. Journal of the American Ceramic Society, 108 (2). e20172. ISSN 0002-7820

https://doi.org/10.1111/jace.20172

Received: 28 May 2024 | Revised: 27 August 2024 | Accepted: 6 September 2024

DOI: 10.1111/jace.20172

Journal of the American Ceramic Society

RESEARCH ARTICLE

Effect of pressure, temperature, and particle size on cold sintered ZnO for transparent thick films on polymer substrates

C. A. Button[1] | **E. Mantheakis**[1] | **G. Wang**[2] | **I. M. Reaney**[1]

[1]Department of Materials Science and Engineering, University of Sheffield, Sheffield, UK

[2]Department of Materials, The University of Manchester, Manchester, UK

Correspondence
Chloe Ariadne Button, Department of Materials Science and Engineering, University of Sheffield, Sheffield, UK.
Email: c.a.button@sheffield.ac.uk

Funding information
Engineering and Physical Sciences Research Council

Abstract

The role of pressure, temperature, and particle size on cold sintering of ZnO has been investigated with a view to developing transparent thick films for device applications. Coarse ZnO (~90–250 nm, cZnO) particles exhibited equiaxed grain growth under all conditions eventually achieving grain sizes of ~ 0.5–1.0 µm at 300°C/375 MPa. In contrast, nano-ZnO (40–80 nm, nZnO), exhibited grain growth along the *c*-axis with a broader grain size distribution (0.5–4 µm) at higher temperatures and pressure (300°C/375 MPa) than cZnO. The broader grain size distribution is attributed to greater dissolution for nZnO compared with cZnO coupled with redistribution of Zn acetate/acetic acid into pores. ZnO continues to dissolve and reprecipitate within the pores throughout the densification process resulting in localized, larger grain sizes. In plane grain growth normal to the pressing direction was observed at and near the sample surface particularly in nZnO, which is attributed to constrained-sintering. Some abnormal grain growth (10–20 µm) was also sporadically observed near or at the surface of nZnO (300°C/375 MPa) due to greater rates of reprecipitation as the transient solvent volatilizes adjacent to the die wall/plunger. Tape casting was used to fabricate single and multiple layers (≈30 µm) of ZnO on Kapton® to demonstrate the potential for device fabrication. Transparency was achieved by choosing cold sintering conditions (200°C/250 MPa) for nZnO that gave ~95% relative density while restricting a majority of grain growth to <200 nm so that internal light scattering from grain boundaries was avoided.

KEYWORDS
cold sintering, low temperature sintering, thick films, transparent conducting oxides, zinc oxide

---

1 | INTRODUCTION

The successful densification of most powdered ceramic materials requires sintering temperatures 0.5–0.75 of the melting temperature (T_m) in °C to achieve a high relative density. This often leads to processing temperatures in excess of 1000°C.[1] Such high processing temperatures lead to high energy requirements and severely limit cosintering compatibility with metals, polymers and glass. It is estimated that sintering accounts for ≈30% of total energy costs in the ceramic industry.[2]

Recently, an ultra-low temperature sintering technique was reported and referred to as "cold sintering" in which a target material is combined with a small amount of a 'transient solvent' then die-pressed at ≤300°C.[3,4] The solvent evaporates out of the side of the die and subsequent reprecipitation on the particle surface results in full or near-full density.[5] Early theories focused on a mechanism adapted from liquid phase sintering[6] whilst others described the process as a defect transport based mechanism,[7] and some arguing that there wasn't enough space between grains for dissolution mass-transport to occur.[8] However, the most recent theory proposes a hyper-accelerated "pressure-solution creep" mechanism,[4] prevalent in nature and observed by geologists since the early 1860s.[9] In this mechanism, small amounts of solution are hosted between the grain boundaries, leading to a chemical potential gradient, resulting in a mechanism that can be broken into 3 stages: (i) dissolution, (ii) mass transport, and (iii) precipitation, with each of these stages acting as a rate limiting step, depending on the conditions. Dissolution takes place in zones of high hydrostatic pressure, which produces the driving force for the material to dissolve. In the second stage, dissolved material is transported across the chemical potential gradient to a low-chemical potential zone, before finally precipitating, on the surface of particles/grains.[10] Depending on conditions, deposition can follow a densification or coarsening path, the latter occurring via a mixed-mode process of Ostwald ripening and coalescence. Cold sintering has not only shown to significantly lower energy requirements for densification,[11] but opens up the prospect of cosintering ceramics with materials, previously not compatible, for example, polymers.[12]

Transparent conducting oxides (TCOs) are critical components in an enormous range of electronic applications, from LCD touchscreens to semiconductor lasers.[13] The most popular method for TCO film manufacture is magnetron sputtering, a physical vapor deposition technique with the ability to produce thin-films over a large area. However, it suffers from a low deposition rate and problems with plasma stability.[14] Cold sintering may offer a new method of TCO manufacture not previously explored. One of the most popular TCO materials is indium tin oxide (ITO) due to its superior conduction.[14–16] However, there is a recent push to find a replacement for ITO due to toxicity concerns[17,18] and environmental impact.[19] ZnO doped with either Ga (GZO) or Al (AZO) are two of the promising replacements of ITO due to ZnO being nontoxic, cheap to produce, and easy to source; while being able to achieve high conductivity and transparency.[20,21]

The cold sintering of ZnO was first reported by Funahashi et al.[22] using a range of low molarities of acetic acid. Work was also undertaken by Kang et al.[23] who performed a comprehensive study of the mechanisms of cold sintering of ZnO. A broad study of the effects of pH, ion concentration, temperature, pressure, environmental conditions, and choice of solvent phase were examined. Their work generally supported Funahashi et al.'s findings however, Raman spectroscopy revealed the presence of small amounts of secondary acetate phase. More aggressive solvents such HNO_3 and HCl did not give rise to high densities and the consensus is that Zn^{2+} concentration is the most important factor in achieving high density rather than pH. Thus, later studies have used either Zn acetate[24,25] or most recently formic acid[26,27] as transient solvents. Formic acid results in superior mechanical properties when compared with acetic acid or zinc acetate, owing to its lower thermal stability which encourages faster precipitation and densification.

There are however, still many aspects of cold sintering process that require greater understanding if consistent quality control is to be achieved and the process commercialized.[26] For example, Serrano et al.[28] studied the nanoparticle-microparticle ratio, showing that an increase in nanoparticle volume increased localized disorder, and affected the morphological, structural and physical properties. More recently further work studying the cold sintering mechanisms has developed master sintering curves[29] and *in operando* impedance spectroscopy has been used to undertake in-situ characterization of the cold sintering process.[30]

Here, we further investigate the role of pressure, temperature and particle size on the cold sintering of ZnO. We also demonstrate through the required control of grain size and porosity, proof of concept for the development of transparent thick films of ZnO on the surface of polymer (Kapton®) sheets to illustrate its potential in device/display technology, building on the work of Baker et al.[31] who used cold sintering to produce flexible printed electroceramic devices.

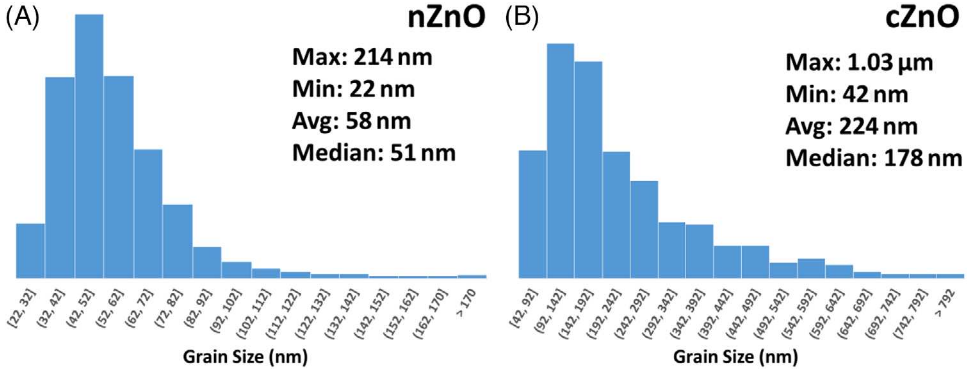

FIGURE 1 Histogram distribution of grain sizes of each of the two powders: (A) nano-Zinc oxide, and (B) a coarser meso-Zinc oxide powder.

2 | EXPERIMENTAL

2.1 | Cold sintering of ZnO ceramics

Nano-ZnO (nZnO) (US Research Nanomaterials Inc., >99% pure) with a spherical morphology had a majority particle size of 30–80 nm, with a small number of particles (total <10%) in size ranges of 20–30 nm and 80–214 nm. "Coarse" ZnO (cZnO) (Sigma Aldrich, 99.9% pure) quoted as <5 µm particle size was decreased by mechanical ball-milling with 10 mm alumina media. Measurement determined the processed cZnO starting powder to have a much more varied and elongated morphology compared to nZnO, with a broader particle size range. ≈90% of the particles falling into the 70–370 nm range with a total of <10% of particles in the 40–70 nm and 370–670 nm range, and ~1% as much larger particles at 0.67–1.03 µm. Histograms of this particle size distribution of starting powders are given in Figure 1.

0.5 g of ZnO powder was combined with ≈20 (cZnO), or ≈30 wt% (nZnO), 1.0 molar acetic acid, and mixed continuously in a pestle and mortar to a fine powder. The powder was poured into a 10 mm die, and pressed at either ≈190, 250, or 375 MPa at room temperature for 10 min. While maintaining pressure, the temperature was raised to either 125, 200, or 300°C, and held 1 h before being cooled using a 20 mm fan to room temperature. Heating and cooling rate was not controlled but was estimated to be between 20 and 40°C/min. Some samples were heat treated for 8 h at 500°C in air with a 5°C/min ramp to remove residual acetate groups. Densities of all samples (unpolished) were calculated via the geometric method and compared to theoretical method.[32]

Undoped ZnO samples were successfully densified across all tested temperatures and pressures similar to previous studies.[22,23] However, early work was initially difficult to repeat until the apparatus was moved to a fume cupboard. This leads to a stable environment with the laminar airflow drawing away accrued moisture, resulting in ceramics with much better handling characteristics, consistent with previous observations by Lowum et al.[25]

2.2 | Fabrication of transparent ZnO thick films

Transparent ZnO thick film was fabricated using tape casting with a water-based formula (Polymer Innovations, Inc.) consisted of plasticizer (PL005), dispersant (DS001), defoamer (DF002), binder (WB4104), distilled water and nZnO powder. This mixture was placed into a speed mixer for 5 min at 1000 rpm, 2 min at 1200 rpm, and 4 min at 1400 rpm to produce a slurry of the desired consistency. The slurry was allowed to de-gas in air for 2 h, before being cast over the surface of an A4 sheet of 50 µm-thick Kapton film and allowed to dry. 1″ circular sections of the tape/Kapton were cut out. The binder was then burned-out in a furnace at 300°C over 20 h with a ramp rate of 0.1°C/min. Post-binder burnout, 25 µL of 1.0 M acetic acid was pipetted onto the surface of the samples before being placed into a die, where the sample was heated to 200°C under 250 MPa to densify nZnO. To maximize adhesion, the Kapton layer was cleaned using isopropanol, and 5 mm PTFE pucks were positioned on either side of the sample in the die to avoid heat degradation.

2.3 | Characterization

X-ray diffraction for phase analysis was performed from $10 \leq 2\theta \leq 90°$ on a Bruker D2 Phaser using CuK_α ($\lambda = 1.5419$ Å) with a step of 0.02°. Raman spectroscopy was carried using a 20MW 514.5 nm green laser on a Renishaw InVia microscope calibrated using a manufacturer supplied Si

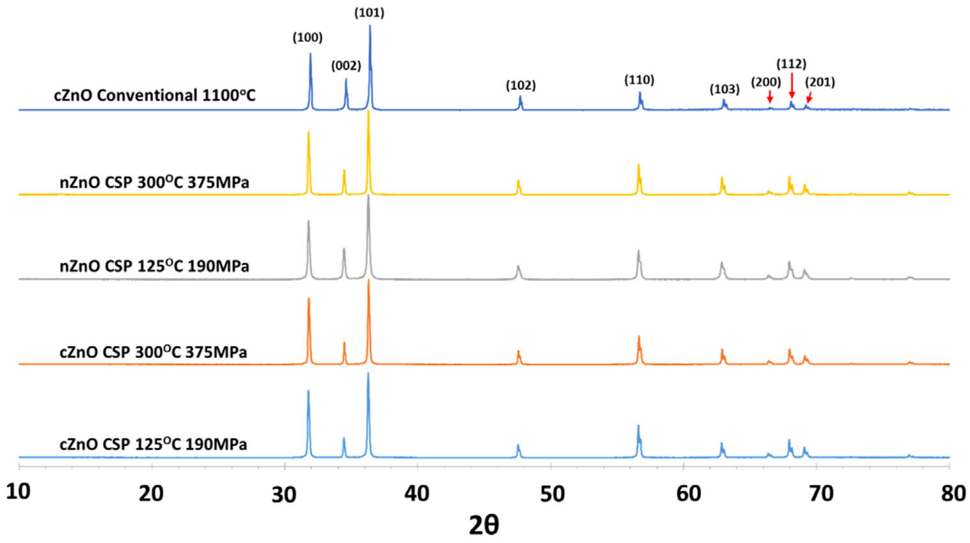

FIGURE 2 X-ray diffraction (XRD) of the two different ZnO powders conventionally and cold sintered under various conditions.

wafer. Scanning electron microscopy images (SEM) were obtained using an FEI Inspect F50 equipped with energy dispersive X-ray analysis at 10 kV and 3.5 spot size from fracture and top surfaces of samples mounted and coated in either gold or carbon. Grain sizes measured using SEM fracture surface and top surface images were obtained from a minimum of 500 grains across 2 areas per sample using ImageJ software.

Cross sections of Kapton-ZnO samples were cold-mounted in epoxy-resin, before being ground with 400, 800, 1200, 2000 silicon carbide paper, followed by polishing with 6, 3, and 1 µm diamond paste. Samples were then sputter coated with gold.

3 | RESULTS AND DISCUSSION

3.1 | Cold sintering of bulk ZnO

The color of cold sintered samples at lower temperatures (<300°C) ranged from yellow to green but a persistent green color was observed at 300°C. This color change has been previously associated with high concentrations of oxygen vacancies (V_O), resulting in F-centers, formed by reduction[33,34] and consistent with Gonzalez-Julian et al.[7] who reported their presence in cold sintered ZnO.

Figure 2 shows the X-ray diffraction (XRD) patterns for ZnO powder, cold and conventionally sintered. X-ray data agreed with available literature[7,22,23] and displayed the expected wurtzite structure for all samples without any peaks for an acetate phase. Its absence in XRD suggests that either the volume fraction of residual acetate is below the detection limit of the diffractometer under the described conditions of operation or the phase is absent.

The hexagonal wurtzite structure of ZnO belongs to the $P6_3mc$ space group made up of 2 group units per unit cell. This gives an irreducible symmetry representation of:

$$\Gamma^{P6-3-mc} = A1 + E1 + 2E2 + 2B1$$

where, only the A_1 and E_1 polar modes and E_2 modes are Raman active.[35,36] Raman spectra from cold sintered samples (Figure 3) agree with available literature across[23,28,36] and compares well with conventionally sintered ZnO. Intense modes at ≈99 and 438 cm^1 correspond to $E\text{-}_2{}^{low}$ and $E_2{}^{high}$ respectively. $E_2{}^{low}$ is influenced by Zn sublattice vibrations, and $E_2{}^{high}$ by oxygen vibration.[35] Several modes are prescribed to second-order modes, including the E_2/A_1 at 328 cm^{-1}, A_1-(TO at 372 cm^{-1}, A_1 at ≈541 cm^{-1}, $A_{1(LO)}$ at ≈569 cm^{-1}, and $E_{1(LO)}$ at ≈585 cm^{-1}. The last 2 of these modes dominantly arise from second-order background, but can be influenced by impurities, particularly $E_{1(LO)}$.[35,37] Two modes form one extended broad peak at 1094 cm^{-1} and 1146 cm^{-1}. The former is a TO+LO mode at M and L Brillouin points. The latter is a combination of $2A_1$(LO), $2E_1$(LO), and 2LO modes occurring at the center point (Γ) of the Brillouin zone.[37]

A single weak secondary acetate phase was observed previously[23,24,38] in Raman studies with 4 modes caused by symmetric stretching of C–C bonds at ≈950 cm^{-1}, C–O at ≈1400 cm^{-1}, C = O at ≈1600 cm^{-1}, and C–H at ≈3000 cm^{-1}. From available data,[39,40] acetate is expected to be removed at 300°C which is above its decomposition temperature. However, acetate was repeatedly observed in 300°C samples possibly due to the limited time at temperature which prevents total decomposition. Heat treatment at 500°C completely removed the acetate but also caused increased expression of second order A_1 and E_1 modes at

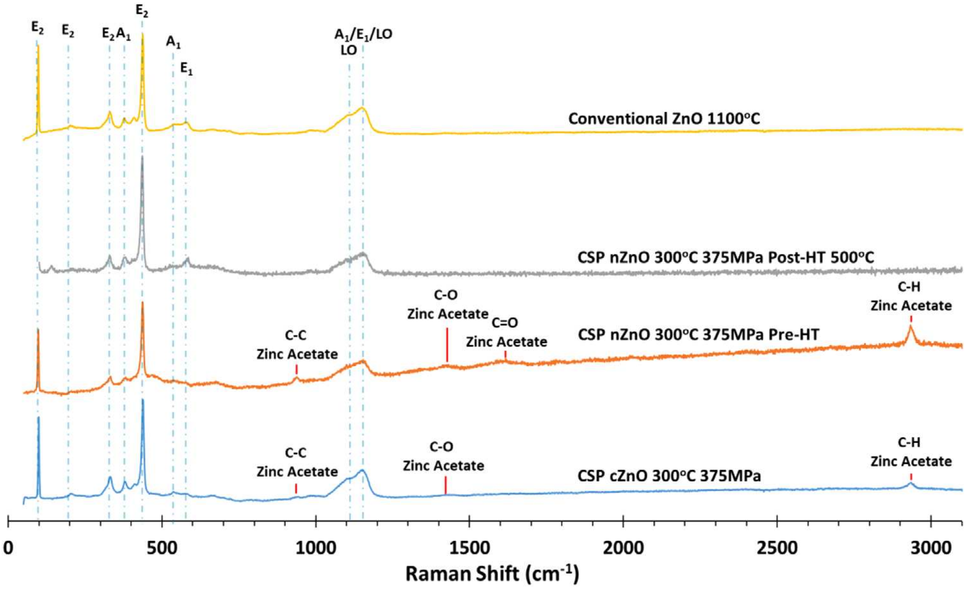

FIGURE 3 Raman spectroscopy shows the presence of the acetate phase in cold sintered samples. Following 500°C heat treatment it shows complete removal.

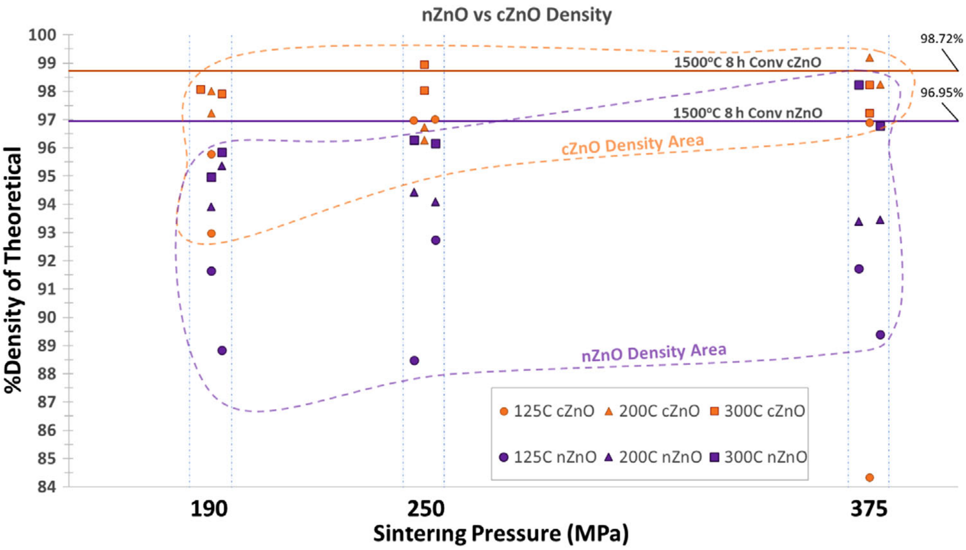

FIGURE 4 Density comparison of nano-ZnO (nZnO) and coarse ZnO (cZnO) at various cold sintering pressures and temperatures compared to conventional. nZnO showed a significantly broader density range which is thought to relate to an increased sensitivity to processing parameters that often occurs when densifying nanomaterials.

≈580 and ≈586 cm^{-1}, respectively. These modes relate to *c*-axis Zn–O bond vibrations and are influenced by the O stoichiometry of the samples.

Figure 4 summarizes the density of cold sintered samples under a range of experimental conditions. Relative densities of >90% theoretical were achieved for all samples with >95% for samples cold sintered at 300°C and ≥250 MPa and conventionally sintered materials. Densities of cZnO were higher than nZnO in conventional sintering and cold sintering, consistent with Serrano et al.[28] Temperature had a greater impact on the final density than pressure which showed little effect on cZnO or nZnO at <300°C. At 300°C, a modest increase in density with increasing pressure is noted in nZnO compared to cZnO, for which density remained largely constant. At 125°C, density varied greatly with little reproducibility in the data. Overall, densities broadly match those reported by Funahashi et al.[22] and Kang et al.[23] who employed starting powders with similar particle size (≈200 nm) to cZnO. Although nZnO has a smaller primary particle size and

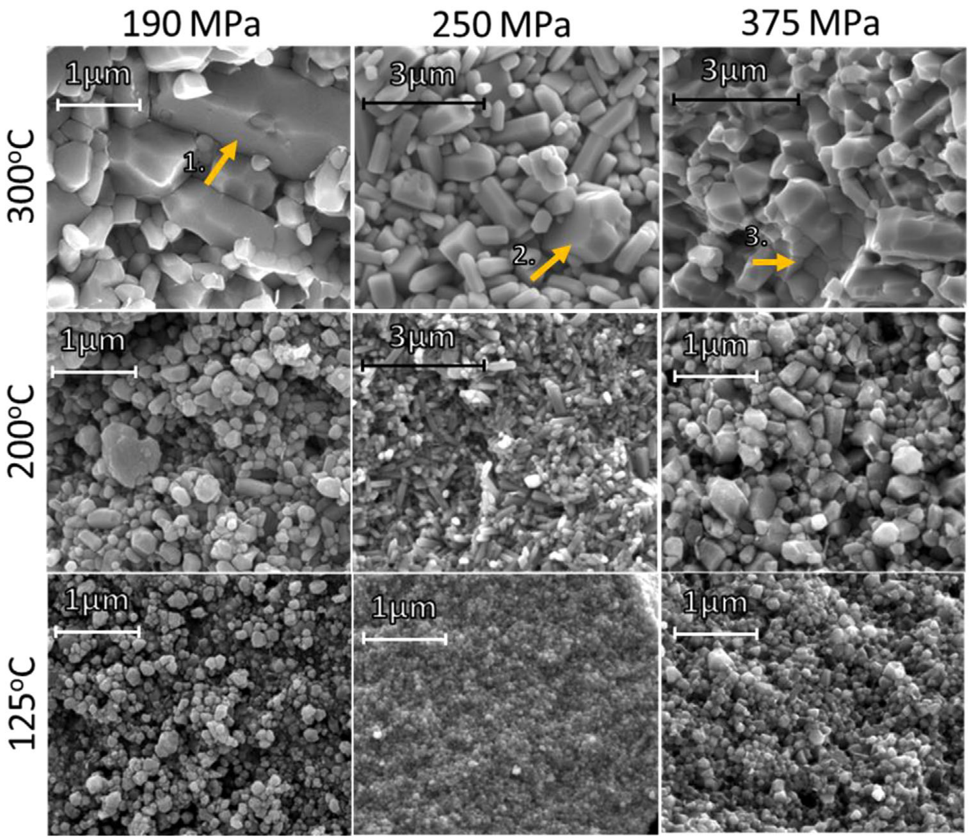

FIGURE 5 Fracture surface scanning electron microscopic (SEM) images of cold sintered nZnO showing significant growth and elongation of grains with increasing temperature and pressure. Arrows 1 and 2 indicate grain growth observed in some areas of samples at 300°C. Arrow 3 highlights triple points.

therefore a higher driving force for sintering compared to cZnO due to its much higher surface energy, there is greater agglomeration,[41] which counteracts the advantages associated with smaller primary particles.

Figures 5 and 6 show SEM images selected from the nZnO and cZnO sample sets, respectively, as described in Figure 3 whereas Figure 7 compares fracture surfaces of optimized cold with conventionally sintered samples. Conventionally sintered cZnO showed closely packed elongated grains of 18–20 μm, with large intragranular pores of 1–3 μm, and smaller intragranular pores of 300–600 nm. Similarly, conventional sintered nZnO also showed a continuous, dense microstructure but with a wider grain size distribution of 5–20 μm, and larger numbers of intragranular pores ranging from 100 to 500 nm in diameter. Figure 8 graphically depicts the grain size distribution for all cold sintered samples in which the grain size distribution increases with temperature for both cZnO and nZnO and the median grain size remains close to the mean for both materials and nearly all conditions (Figure 8).

At 125°C 190 MPa, no grain growth was observed in either nZnO or cZnO, however some densification occurred, with SEM images showing intergranular contacts (triple points). As temperature increased, the grain size for nZnO and cZnO increased while retaining a narrow grain size distribution. At 300°C for cZnO, grain size was 285 nm (±144) 190 MPa and increased to 505 nm (±330) and 538 nm (±458) to 250 MPa and 375 MPa, respectively. Although the average grain size increased only slightly with from 250 to 375 MPa at 300°C for cZnO, the mean grain size for cZnO became much larger than the median, indicating a greater population of larger grains, supporting the premise of a more inhomogeneous microstructure.

For nZnO, at 300°C, grain size and distribution increased to 733 nm at 375 MPa compared to cZnO (458 nm) under the same conditions. The majority of cZnO and nZnO pellets showed no signs of in plane grain growth within their interior normal to the pressing direction. However, at or near the surfaces, both materials showed in-plane grain growth, especially at higher pressures. This is attributed to “constrained sintering”, a common feature of pressure sintering technology.[8,14,41]

Microstructures observed in cZnO samples compare well to those of Funahashi et al.[22] and Kang et al.[23] However, our results show that the effect of pressure is understated by these authors when cold sintering at

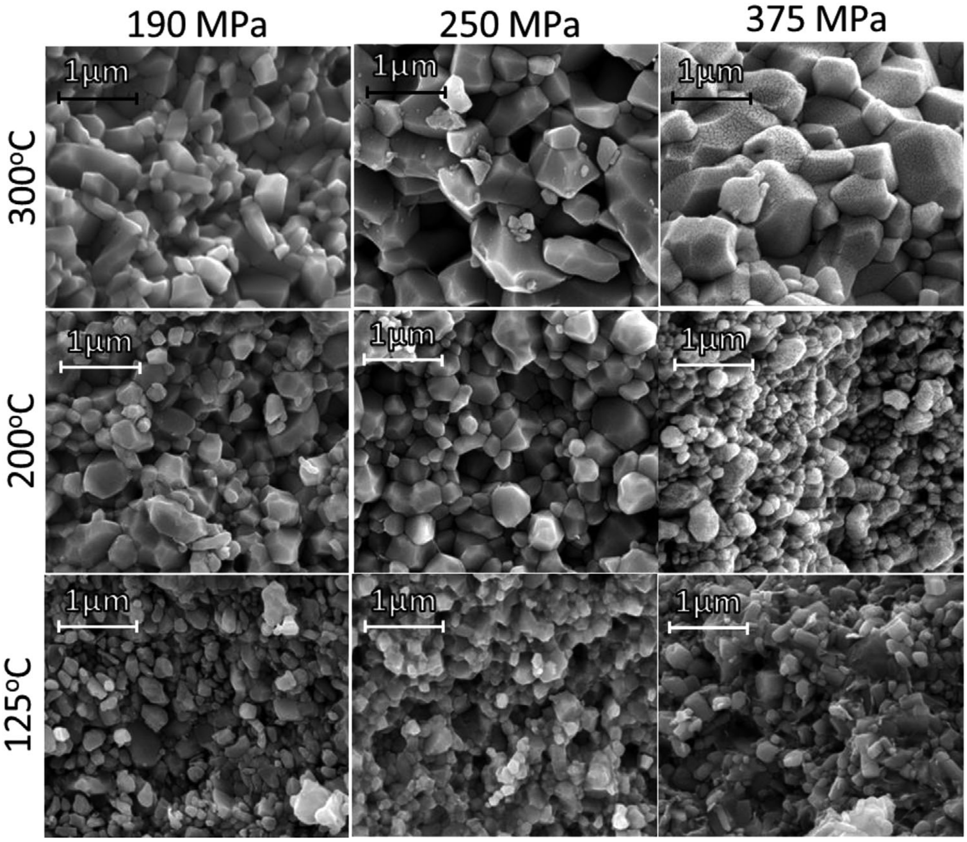

FIGURE 6 Fracture surface scanning electron microscopic (SEM) images of cZnO showing lower grain growth until 300°C and a consistent equiaxed grain morphology with respect to nZnO.

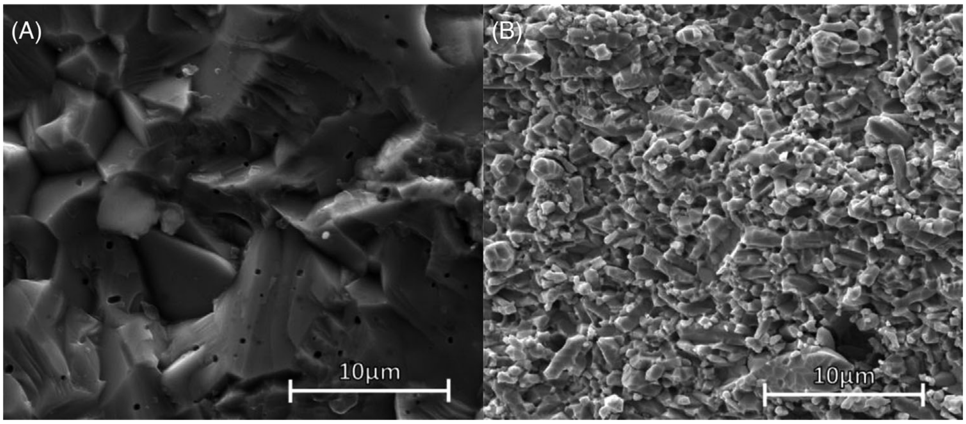

FIGURE 7 Fracture surface scanning electron microscopy (SEM) of nZnO: (A) conventionally sintered at 1500°C, and (B) cold sintered at 300°C, 375 MPa.

higher temperatures (e.g., 300°C) with particularly nZnO exhibiting a broader grain-size distribution with increasing pressure. Grain growth and broad grain size distributions are common problems in the sintering of nanopowders, which even without the presence of liquid phase, are sensitive to factors such as heating rate.[41] In addition, pressure impacts on grain morphology with nZnO (Figure 5) equiaxed until 300°C at low pressures but at 250 MPa grain growth is initiated at 200°C with the formation of elongated grains. In contrast, cZnO (Figure 6) remained dominantly equiaxed at all pressures and temperatures.

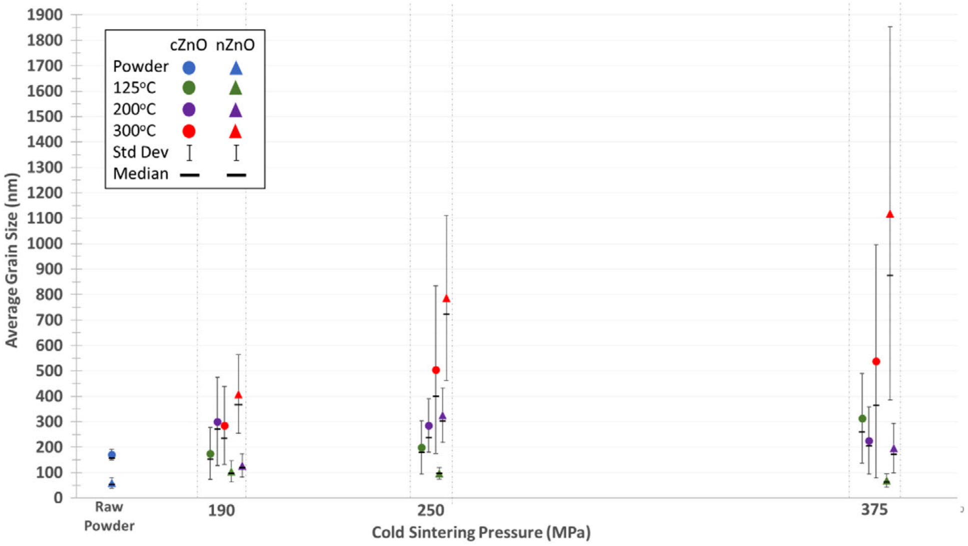

FIGURE 8 Grain size distribution measured on the fracture surfaces of cold sintered cZnO and nZnO. Grain size distribution remains stable with increase in pressure at lower temperatures. However, grain size distribution increases for both materials (especially nZnO) with increase in pressure at 300°C.

The difference in the grain morphology between nZnO and cZnO are attributed to a number of factors. The greater surface to volume ratio in nano (nZnO) compared with meso (cZnO) particles leads to greater dissolution and possibly total dissolution of some of the ZnO particles (nZnO has a surface area ~3*x* that of the cZnO powder). The rapid increase in grain size distribution at 300°C may be attributed to the much higher occurrence of breakdown of the zinc acetate complex[27] when combined with the rapid heating rate is hypothesized to cause a thermal decomposition process in which Zn ions rapidly precipitate out of solution as the acetate phase decomposes and deposit locally. The form of deposition (heterogeneous or homogeneous[3]) depends on what is most energetically favorable. Higher pressures leading to higher levels of supersaturation and thus higher concentrations of Zn deposition thus leading to a larger grain size distribution. This effect at 300°C, compounded by the higher pressure, may not only lead to greater dissolution and thus supersaturation, but also Zn acetate/acetic acid being progressively forced into fewer and fewer remaining pores as densification proceeds. Overall, these experiments imply that while high densities can be achieved across multiple conditions, if cold sintering is to reach commercialization, much better control of processing is required to optimize grain size distributions and morphology.

3.2 | Abnormal grain growth

Although a conventional grain structure with a monomodal distribution was routinely observed for nearly all samples, a minority exhibited microstructures with evidence of abnormal grain growth, particularly for nZnO. These may be separated into either individual abnormally large 'super' grains in a matrix of smaller grains (Figure 9A), or regions of larger grains with nanograins decorating their grain boundaries (Figure 9B) giving a 'cobblestone' appearance. The former appeared infrequently throughout samples but most commonly at the surface, the latter was observed almost exclusively very near to/or as a surface microstructure.

Regions of larger grains are not an uncommon feature in the conventional sintering of nano-powders. They have previously been described to be caused by insufficient breaking up of powder agglomerates before sintering. These agglomerates with better packing are thought to experience accelerated growth leading to these structures. Hynes et al.[42] previously reported similar structures when sintering nanophase ZnO conventionally.

It is thought that the formation of the "cobblestone" structure may be caused by pressure progressively forcing Zn-acetate/acetic acid to the surface where for a protracted period (presumably the entire time to densification) dissolution/reprecipitation occurs, leading to abnormal grain growth. Reprecipitation readily occurs at the surface of the pellet since it is the region where the acetic acid volatilizes and escapes though the gap between plungers, die wall, and sample. This facilitates dissolution and mass transport locally, leading to grain growth. The consistent replenishing of the Zn-acetate/acetic acid rich regions near the surface from the interior, means that these processes continue to encourage grain growth longer, nearer to the surface.

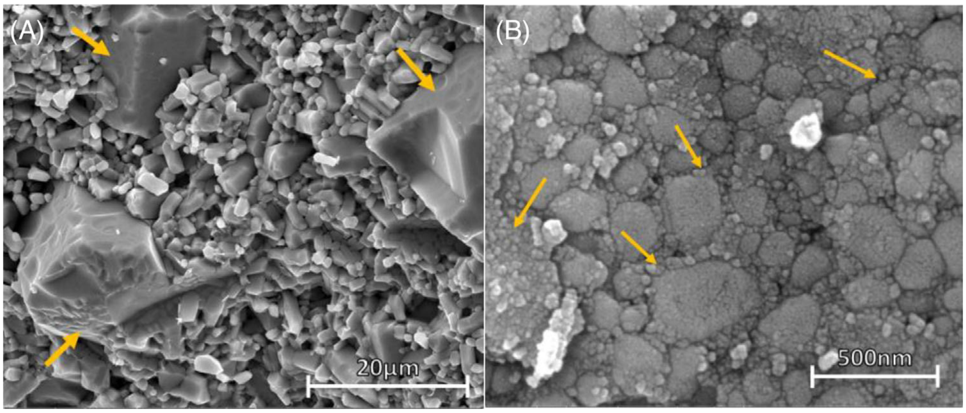

FIGURE 9 Abnormal grain structures sometimes observed in cold sintered nZnO in the form of: (A) super-grain structures (arrowed), and (B) grain boundary nano-grain formation (arrowed).

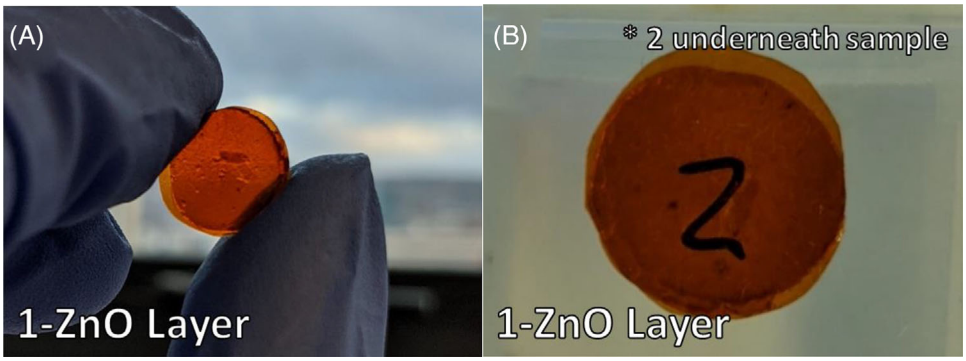

FIGURE 10 (A and B). Transparent layer of ZnO cold sintered between two layers of Kapton. Note the 2 in image B is underneath the sample.

3.3 | Thick film ZnO-Kapton multilayers

Based on the bulk studies described in the above sections. Conditions for cold sintering (200°C, 250 MPa) were chosen for the thick films to ensure densification of the tape cast ZnO layers that were unlikely to induce grain growth (promoting transparency as the grain size/residual pore size would remain less than the wavelength of visible light) and protected the Kapton from charring. Figure 10A,B shows low magnification optical images of a transparent ZnO layer cold-sintered between 2 layers of Kapton. The ZnO was tape cast directly onto Kapton (up to 4 layers) with a 5 mm thick PTFE spacer used to protect the sample from damage during cold sintering.

Single layer composites showed the highest transparency (Figure 10: note the orange coloration is from the Kapton, not the ZnO). Transparency decreased with an increasing number of layers, with samples becoming totally opaque by 4-layers. Adhesion of the ZnO to the Kapton varied and flexing resulted in cracking of the ZnO layer. However, samples would often tear the Kapton before detaching from the ZnO.

XRD patterns revealed peaks associated with the expected wurtzite structure. Narrow peaks were observed in the 1- and 2-layer samples, but broadening was present in 4-layer samples, suggesting a smaller crystallite size. Broad intensities are observed at ≈14°, 22°, and 26° from the amorphous Kapton.

SEM images (Figure 11) revealed mostly faceted, equiaxed nano-grains and a decrease in grain size with increasing layers, consistent with XRD line broadening. One layer samples showed a dense microstructure with a grain size of 154 ±67 nm 2- and 4-layer samples had a grain size range of ≈121 ±51 nm and ≈63 ±28 nm, respectively, with greater porosity (lower density) and less faceted grains, presumably due to the Kapton inhibiting heat transfer which may be solved through further optimization of the heating schedule.

Optical and SEM images of a 2-layer sample in (Figure 12) shows sharp Kapton/ZnO interface with no evidence of interdiffusion or penetration. Detachment of the

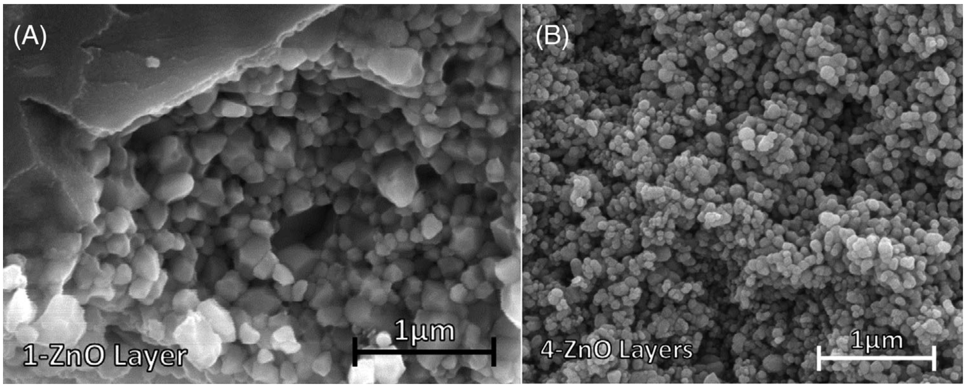

FIGURE 11 Fracture surface scanning electron microscopy (SEM) from ZnO-Kapton composites post cold sintering with (A) 1-layer of ZnO; and (B) 4-layers of ZnO.

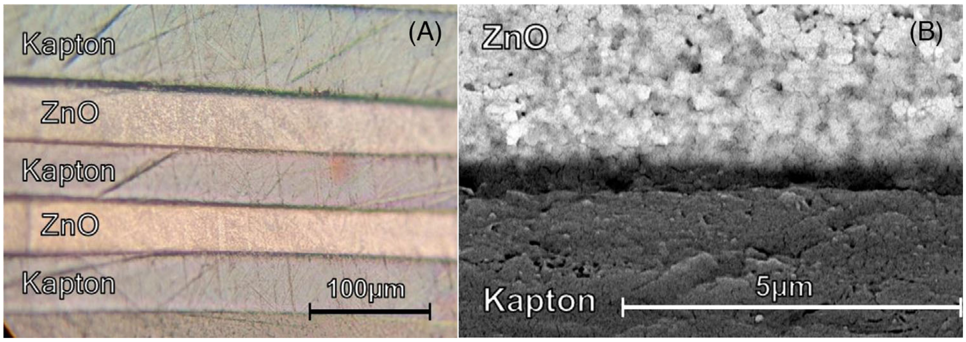

FIGURE 12 Cross sectional optical (A) and scanning electron microscopy (SEM) (B) images showing the sintered layer bonded to the Kapton layers.

top layer of Kapton was resolved by ensuring the Kapton surfaces were thoroughly cleaned.

ZnO layers were therefore successfully deposited by cold sintering using a tape cast process onto a polymer substrate without evidence of deterioration. Moreover, the high density and small grain/particle size of the ZnO ensured that the layers were transparent. There was a slight variation in the thickness of the ZnO layers across the sample shown in Figure 12, a particular layer thickness was not the core aim of this study; rather we aimed to demonstrate proof-of-concept which opens up a large number of potential applications for the development of optic and electro-optic devices and displays. To truly develop this process however, further understanding would require electro-optic measurements and the deposition of thinner layers.

4 | CONCLUSIONS

The role of pressure, temperature, and particle size on the cold sintering of ZnO has been investigated. All sample sintered to >90% dense for all conditions studied with the microstructures of cZnO matching previous findings. Samples cold sintered at 300°C were uniformly green but color variation was observed at lower temperatures. The green color was attributed to the presence of V_O. Raman spectroscopy identified the presence of retained Zn acetate which could be eliminated by heat treatment at 500°C.

Overall, temperature rather than pressure was determined to be the primary parameter in the cold sintering of ZnO, irrespective of particle size. However, at 300°C, increasing pressure promoted greater density of nZnO as well as widening the grain size distribution. Generally, cold sintering of nZnO proved more challenging and samples exhibited abnormal grain growth, particularly near or at the surface. Using conditions that densified bulk samples but restricted grain growth (200°C/250 MPa), thereby minimizing internal light scattering, cold sintered, tape cast layers of transparent ZnO were deposited on Kapton, opening up the possibility for the fabrication of optic and electro-optic devices and displays in the future.

ACKNOWLEDGMENTS

This work was supported by the Engineering and Physical Sciences Research Council, EP/X016463/1.

ORCID

C. A. Button https://orcid.org/0009-0005-2070-9548
G. Wang https://orcid.org/0000-0003-0125-454X

REFERENCES

1. Rahman MN. Ceramic Processing and Sintering. New York: Marcel Dekker Inc.; 1995.
2. Furszyfer DD, Sovacool BK, Foley AM, Griffiths S, Bazilian M, Kim J, et al. Decarbonizing the ceramics industry: a systematic and critical review of policy options, developments and sociotechnical systems. Renew Sustain Energy Rev. 2022;157:112081. https://doi.org/10.1016/j.rser.2022.112081
3. Maria JP, Kang X, Floyd RD, Dickey EC, Guo H, Guo J, et al. Cold sintering: current status and prospects. J Mater Res. 2017;32(17):3205–18. https://doi.org/10.1557/jmr.2017.262
4. Ndayishimiye A, Bang SH, Spiers CJ, Randall CA. Reassessing cold sintering in the framework of pressure solution theory. J Eur Ceram Soc. 2022;43:1–13. https://doi.org/10.1016/j.jeurceramsoc.2022.09.053
5. Galotta A, Sglavo VM. The cold sintering process: a review on processing features, densification mechanisms and perspectives. J Eur Ceram Soc. 2021;41(16):1–17. https://doi.org/10.1016/j.jeurceramsoc.2021.09.024
6. Guo J, Guo H, Baker AL, Lanagan MT, Kupp ER, Messing GL, et al. Cold sintering: a paradigm shift for processing and integration of ceramics. Angew Chemie—Int Ed. 2016;55(38):11457–61. https://doi.org/10.1002/anie.201605443
7. Gonzalez-Julian J, Neuhaus K, Bernemann M, Pereira Da Silva J, Laptev A, Bram M, et al. Unveiling the mechanisms of cold sintering of ZnO at 250°C by varying applied stress and characterizing grain boundaries by Kelvin probe force microscopy. Acta Mater. 2018;144:116–28. https://doi.org/10.1016/j.actamat.2017.10.055
8. Biesuz M, Taveri G, Duff AI, Olevsky E, Zhu D, Hu C, et al. A theoretical analysis of cold sintering. Adv Appl Ceram. 2020;119(2):75–89. https://doi.org/10.1080/17436753.2019.1692173
9. Sorby HC. The Bakerian lecture— on the direct correlation of mechanical and chemical forces. Proceed Royal Soc London. 1863;xxiii(1861):538–50.
10. Shimizu I. Kinetics of pressure solution creep in quartz: theoretical considerations. Tectonophysics. 1995;245(3–4):121–34. https://doi.org/10.1016/0040-1951(94)00230-7
11. Sohrabi Baba Heidary D, Lanagan M, Randall CA. Contrasting energy efficiency in various ceramic sintering processes. J Eur Ceram Soc. 2018;38(4):1018–29. https://doi.org/10.1016/j.jeurceramsoc.2017.10.015
12. Zhao X, Guo J, Wang K, Herisson De Beauvoir T, Li B, Randall CA. Introducing a ZnO–PTFE (polymer) nanocomposite varistor via the cold sintering process. Adv Eng Mater. 2018;20(7):1–8. https://doi.org/10.1002/adem.201700902
13. Afre RA, Sharma N, Sharon M, Sharon M. Transparent conducting oxide films for various applications: a review. Rev Adv Mater Sci. 2018;53(1):79–89. https://doi.org/10.1515/rams-2018-0006
14. Exarhos GJ, Zhou XD. Discovery-based design of transparent conducting oxide films. Thin Solid Film. 2007;515(18):7025–52. https://doi.org/10.1016/j.tsf.2007.03.014
15. Singh C, Panda E. Variation of electrical properties in thickening Al-doped ZnO films: role of defect chemistry. RSC Adv. 2016;6(54):48910–8. https://doi.org/10.1039/c6ra06513a
16. Chen Z, Li W, Li R, Zhang Y, Xu G, Cheng H. Fabrication of highly transparent and conductive indium-tin oxide thin films with a high figure of merit via solution processing. Langmuir. 2013;29(45):13836–42. https://doi.org/10.1021/la4033282
17. Homma T, Ueno T, Sekizawa K, Tanaka A, Hirata M. Interstitial pneumonia developed in a worker dealing with particles containing indium-tin oxide. J Occup Health. 2003;45(3):137–9. https://doi.org/10.1539/joh.45.137
18. Badding MA, Fix NR, Orandle MS, Barger MW, Dunnick KM, Cummings KJ, et al. Pulmonary toxicity of indium-tin oxide production facility particles in rats. J Appl Toxicol. 2016;36(4):618–26. https://doi.org/10.1002/jat.3253
19. Zhang K, Wu Y, Wang W, Li B, Zhang Y, Zuo T. Recycling indium from waste LCDs: A review. Resour Conserv Recycl. 2015;104(100):276–90. https://doi.org/10.1016/j.resconrec.2015.07.015
20. Gallium price. Strategic Metal Investments Ltd, 2014.
21. Aluminium commodity price live. Business Insider: Markets. 2020.
22. Funahashi S, Guo J, Guo H, Wang Ke, Baker AL, Shiratsuyu K, et al. Demonstration of the cold sintering process study for the densification and grain growth of ZnO ceramics. J Am Ceram Soc. 2017;100(2):546–53. https://doi.org/10.1111/jace.14617
23. Kang X, Floyd R, Lowum S, Cabral M, Dickey E, Maria JP. Mechanism studies of hydrothermal cold sintering of zinc oxide at near room temperature. J Am Ceram Soc. 2019;102(8):4459–69. https://doi.org/10.1111/jace.16340
24. Floyd RD, Lowum S, Maria JP. Cold sintering zinc oxide with a crystalline zinc acetate dihydrate mass transport phase. J Mater Sci. 2020;55(31):15117–29. https://doi.org/10.1007/s10853-020-05100-9
25. Lowum S, Floyd R, Bermejo R, Maria JP. Mechanical strength of cold-sintered zinc oxide under biaxial bending. J Mater Sci. 2019;54(6):4518–22. https://doi.org/10.1007/s10853-018-3173-8
26. Jabr A, Jones HN, Argüelles AP, Trolier-McKinstry S, Randall C, Bermejo R. Scaling up the cold sintering process of ceramics. J Eur Ceram Soc. 2023;43(12):5319–29. https://doi.org/10.1016/j.jeurceramsoc.2023.04.061
27. Jabr A, Fanghanel J, Fan Z, Bermejo R, Randall C. The effect of liquid phase chemistry on the densification and strength of cold sintered ZnO. J Eur Ceram Soc. 2023;43(4):1531–41. https://doi.org/10.1016/j.jeurceramsoc.2022.11.071
28. Serrano A, Caballero-Calero O, García MÁ, Lazić S, Carmona N, Castro GR, et al. Cold sintering process of ZnO ceramics: effect of the nanoparticle/microparticle ratio. J Eur Ceram Soc. 2020;40(15):5535–42. https://doi.org/10.1016/j.jeurceramsoc.2020.05.059
29. Albar N, Hérisson de Beauvoir T, Bouyat A, Chevallier G, Weibel A, Estournès C. Master sintering curve analysis of ZnO densified by cold sintering process. Open Ceram. 2024;18:0–5. https://doi.org/10.1016/j.oceram.2024.100593
30. Hérisson de Beauvoir T, Taberna PL, Simon P, Estournès C. Cold Sintering Process characterization by in operando electrochemical impedance spectroscopy. J Eur Ceram Soc. 2022;42(13):5747–55. https://doi.org/10.1016/j.jeurceramsoc.2022.05.077
31. Baker A, Guo H, Guo J, Randall C, Green DJ. Utilizing the Cold Sintering Process for Flexible–Printable Electroceramic Device Fabrication. J Am Ceram Soc. 2016;99(10):3202–4. https://doi.org/10.1111/jace.14467

32. Rumble J. CRC_Press. CRC handbook of chemistry and physics. 102nd ed. Boca Raton, Florida: CRC Press; 2020.
33. Leiter F, Alves H, Pfisterer D, Romanov NG, Hofmann DM, Meyer BK. Oxygen vacancies in ZnO. Phys B Condens Matter. 2003;340–342:201–4. https://doi.org/10.1016/j.physb.2003.09.031
34. Vanheusden K, Warren WL, Seager CH, Tallant DR, Voigt JA, Gnade BE. Mechanisms behind green photoluminescence in ZnO phosphor powders. J Appl Phys. 1996;79(10):7983–90. https://doi.org/10.1063/1.362349
35. Šćepanović M, Grujić-Brojčin M, Vojisavljević K, Bernikc S, Srećković T. Raman study of structural disorder in ZnO nanopowders. J Raman Spectrosc. 2010;41(9):914–21. https://doi.org/10.1002/jrs.2546
36. De S E Silva RL, Franco A. Raman spectroscopy study of structural disorder degree of ZnO ceramics. Mater Sci Semicond Process. 2020;119:105227. https://doi.org/10.1016/j.mssp.2020.105227
37. Cuscó R, Grujić-Brojčin M, Vojisavljević K, Bernik S, Srećković T. Temperature dependence of Raman scattering in ZnO. Phys Rev B—Condens Matter Mater Phys. 2007;75(16):165202. https://doi.org/10.1103/PhysRevB.75.165202
38. Ndayishimiye A, Sengul MY, Bang SH, Tsuji K, Takashima K, Hérisson De Beauvoir T, et al. Comparing hydrothermal sintering and cold sintering process: Mechanisms, microstructure, kinetics and chemistry. J Eur Ceram Soc. 2020;40(4):1312–24. https://doi.org/10.1016/j.jeurceramsoc.2019.11.049
39. Ghule AV, Ghule K, Chen CY, Chen WY, Tzing SH, Chang H, et al. In situ thermo-TOF-SIMS study of thermal decomposition of zinc acetate dihydrate. J Mass Spectrom. 2004;39(10):1202–8. https://doi.org/10.1002/jms.721
40. Ghule AV, Lo B, Tzing SH, Ghule K, Chang H, Ling YC. Simultaneous thermogravimetric analysis and in situ thermo-Raman spectroscopic investigation of thermal decomposition of zinc acetate dihydrate forming zinc oxide nanoparticles. Chem Phys Lett. 2003;381(3–4):262–70. https://doi.org/10.1016/j.cplett.2003.09.125
41. Lu K. Sintering of nanoceramics. Int Mater Rev. 2008;53(1):21–38. https://doi.org/10.1179/174328008İ254358
42. Hynes AP, Doremus RH, Siegel RW. Sintering and characterization of nanophase zinc oxide. J Am Ceram Soc. 2002;85(8):1979–87. https://doi.org/10.1111/j.1151-2916.2002.tb00391.x

How to cite this article: Button CA, Mantheakis E, Wang G, Reaney IM. Effect of pressure, temperature, and particle size on cold sintered ZnO for transparent thick films on polymer substrates. J Am Ceram Soc. 2024;e20172. https://doi.org/10.1111/jace.20172